

# Single-Step Spray Printing of Symmetric All-Organic Solid-State Batteries Based on Porous Textile Dye Electrodes

Puiki Leung,\* Junfu Bu, Pablo Quijano Velasco, Matthew R. Roberts, Nicole Grobert, and Patrick S. Grant\*

A symmetric solid-state battery based on organic porous electrodes is fabricated using scalable spray-printing. The active electrode material is based on a textile dye (disperse blue 134 anthraquinone) and is capable of forming divalent cations and anions in oxidation and reduction processes. The resulting molecule can be used in both negative and positive electrode reactions. After spray printing an inter-connected pore honeycomb electrode, a solid-state electrolyte ( $\sigma_{Li^+} \times 10^{-4} \text{ S cm}^{-1}$ ) based on a polymeric ionic liquid is spray-printed as a second layer and infiltrated through the porous electrodes. A symmetric all-organic battery is then formed with the addition of another identical set of electrode and electrolyte layers. Both density functional theory calculations and charge-discharge profiles show that the potentials for the negative and positive electrode reactions are amongst the lowest ( $\approx 2.0 \text{ V vs Li}$ ) and the highest ( $\approx 3.5 \text{ V vs Li}$ ), respectively, for quinone-type molecules. Over the C-rate range 0.2 to 5 C, the battery has a discharge cell voltage of more than 1 V even up to 250 charge-discharge cycles and capacities are in the range 50–80 mA h g<sup>-1</sup> at 0.5 C.

highly energetic short circuit discharge.<sup>[1]</sup> An alternative inherently safer (albeit lower gravimetric density) approach is to combine solid-state polymer electrolytes and organic electrodes in a rechargeable configuration based only on organic materials, with no prospect for the problems associated with Li plating/dendrites.<sup>[2]</sup>

Solid-state all-organic batteries are composed of naturally abundant chemical elements (C, H, N, O, S, and F) and have the potential to be synthesized from renewable resources. Organic compounds are often low-cost and have various electrochemical properties, relieving the environmental issues associated with the use of transition metals in conventional Li-ion battery electrodes. In terms of battery performance, organic electrochemically active molecules can offer opportunities for tailoring functionalities by adjusting

## 1. Introduction

Solid-state batteries can address some of the suboptimum safety aspects of conventional Li/Na-ion batteries that usually contain flammable and volatile electrolytes. However and despite accelerating progress, this solid-state battery arrangement does not yet fully eradicate safety concerns, primarily due to the tendency for the formation of Li dendrites at the negative electrode that may penetrate the ion conducting separator/electrolyte and cause

the molecular structures using relatively mature and scalable organic synthesis approaches. Organic electrodes usually do not involve ion (de)intercalation reactions, thus potentially pulverizing intercalation strains are avoided, and may allow high charge-discharge rates of up to 100 C (in liquid electrolytes).<sup>[2]</sup> Since the charge storage reaction mechanisms are based on conversion reactions, they are, in principal, electroactive toward any cation, which has been demonstrated for systems containing Li<sup>+</sup>, Na<sup>+</sup>, Mg<sup>2+</sup>, K<sup>+</sup>, and H<sup>+</sup> ions.<sup>[2,3]</sup>

Organic materials for reversible electrode reactions are usually chosen from the three major carbonyl classes: I) quinones, II) imides, and III) conjugated carboxylates.<sup>[2]</sup> Among these groups, quinones and their derivatives are the most studied with Li or Na ion-based electrolytes because of their relatively high electrode potential (i.e., 2–3.2 V) and capacity per unit weight (theoretically up to 600 mA h g<sup>-1</sup>).<sup>[2]</sup> Quinones have been generally explored in the reduction configuration, which converts (reduces) molecules to divalent anions ( $Q \rightarrow Q^{2-}$ ) with reversible electrode potentials <3.4 V versus Li, achieved by incorporating suitable functional groups.<sup>[4]</sup> Radical cations of other organic materials, such as substituted dialkoxylbenzene [i.e., 2,5-di-*tert*-butyl-1,4-bis(2-methoxyethoxy)benzene (DBBB)] and nitroxide [i.e., (2,2,6,6-tetramethylpiperidin-1-yl)oxyl (TEMPO)] radicals have also been proposed to yield higher electrode potentials of up to  $\approx 3.9 \text{ V}$  versus Li.<sup>[5]</sup> As only single electron-transfer is involved in the oxidation of most DBBB or TEMPO based molecules, phenylenediamine-based materials have also been proposed recently as they may provide two

Dr. P. Leung, Dr. J. Bu, P. Quijano Velasco, Prof. N. Grobert, Prof. P. S. Grant  
Department of Materials  
University of Oxford  
Parks Road, Oxford OX1 3PH, UK  
E-mail: Puiki.leung@materials.ox.ac.uk; Patrick.grant@materials.ox.ac.uk

Dr. M. R. Roberts  
Dyson Ltd.  
Tetbury Hill, Malmesbury SN16 0RP, UK  
Prof. N. Grobert  
Williams Advanced Engineering  
Grove, Oxfordshire OX12 0DQ, UK

The ORCID identification number(s) for the author(s) of this article can be found under <https://doi.org/10.1002/aenm.201901418>.

© 2019 The Authors. Published by WILEY-VCH Verlag GmbH & Co. KGaA, Weinheim. This is an open access article under the terms of the Creative Commons Attribution License, which permits use, distribution and reproduction in any medium, provided the original work is properly cited.

DOI: 10.1002/aenm.201901418

electron-transfers reactions. However, these materials have significant challenges in terms of dissolution/exfoliation when used with liquid electrolytes.<sup>[6]</sup>

The oxidation of certain types of anthraquinones (diaminoanthraquinone derivatives) have been reported with high electrode potentials.<sup>[7]</sup> Potash et al.<sup>[8]</sup> demonstrated that diaminoanthraquinones can form stable divalent cations ( $Q \rightarrow Q^{2+}$ ) and thus conceptually could be used as both negative and positive electrodes for reversible reactions in a liquid-based flow battery system. The use of identical electrodes acting as positive and negative electrodes in ion-based storage systems would simplify the manufacturing process, and potentially reduce cost. So far, this type of symmetric ion battery has been limited to electrodes containing vanadates,<sup>[9]</sup> titanates,<sup>[10]</sup> and three types of organic electrodes ( $M_4C_8H_2O_6$ ,<sup>[11]</sup>  $(C_6H_4)_n$ ,<sup>[12]</sup> and  $Na_4C_6O_6$ <sup>[13]</sup>), as summarized in a recent review paper.<sup>[14]</sup>

These types of anthraquinone are already produced at large scale from coal tar residues for wide use as “disperse dyes” in the textile industry.<sup>[8,15]</sup> These dye molecules are not ideal for flow battery applications due to their relatively low solubility (i.e., <0.2 M) compared with other more soluble conventional redox molecules typically used at >1 M.<sup>[16]</sup> However, lower solubility is an advantage for ion battery electrodes where dissolution in the electrolyte can be problematic,<sup>[2]</sup> leading to capacity fade caused by the “redox shuttle” effect.<sup>[2]</sup>

In general, the dissolution of organic molecules in contact with an electrolyte can be partially ameliorated by polymerization of the molecule or/and the use of solid-state electrolytes (SSEs). When a SSE is used, reasonable energy storage performance has been demonstrated for small quinone molecules (i.e., benzoquinone) without polymerization,<sup>[17]</sup> which is beneficial as monomer organic electrodes tend to have higher electrode potentials and electronic conductivities than their polymer counterparts.<sup>[4]</sup> However, as is well known, compared with liquid electrolytes, SSE typical shortcomings are low ionic conductivity, increased and variable interfacial contact resistance, and restricted infiltration into the electrode structure.<sup>[18]</sup>

To address these issues, we introduce a “layer-by-layer” spray printing technique as a route to prepare porous organic electrodes based on widely available, low-cost quinone-type dye molecules with controlled thickness, onto and into which a polymer SSE is then deposited. The polymer SSE is based on a polymeric ionic liquid, which is nonflammable and has reasonably high ionic conductivity ( $\approx 10^{-4}$  S cm<sup>-1</sup>) at room temperature.<sup>[19]</sup> The fabrication of the porous, spray printed electrode makes use of a phase separation/inversion method derived from the preparation of microporous polymers in casting, electrospinning, and electrospraying techniques<sup>[20]</sup> and involves an aqueous suspension of the active material (organic dye) and fine-scale carbon (“carbon black”) in a mixture of two (miscible) fugitive liquids. The differential evaporation of the two liquids,<sup>[20b-d,21,22]</sup> leads to a honeycomb pore structure reproducible over large areas. Schematic representations of the cells studied here are shown in **Figure 1** involving the uses of porous organic electrodes and PIL-based SSEs. Density functional theory (DFT) calculations are used to understand the behaviors of the active quinone molecules at different oxidation states. We evaluated half- and full-cell solid-state configurations (symmetric) using a range of electrochemical techniques under different C-rates at ambient temperatures (i.e.,  $22 \pm 1$  °C). To the best knowledge of the authors, the work is the first to report the performance of a symmetric solid-state battery based entirely on organic electrode and electrolyte materials with more than 1 V.

## 2. Results and Discussion

### 2.1. Density Functional Theory Calculations

Computational calculations of disperse blue 134 and other similar organic molecules (i.e., quinones and phenylenediamine) at different oxidation states were performed using density functional theory. The geometric structures of these molecules

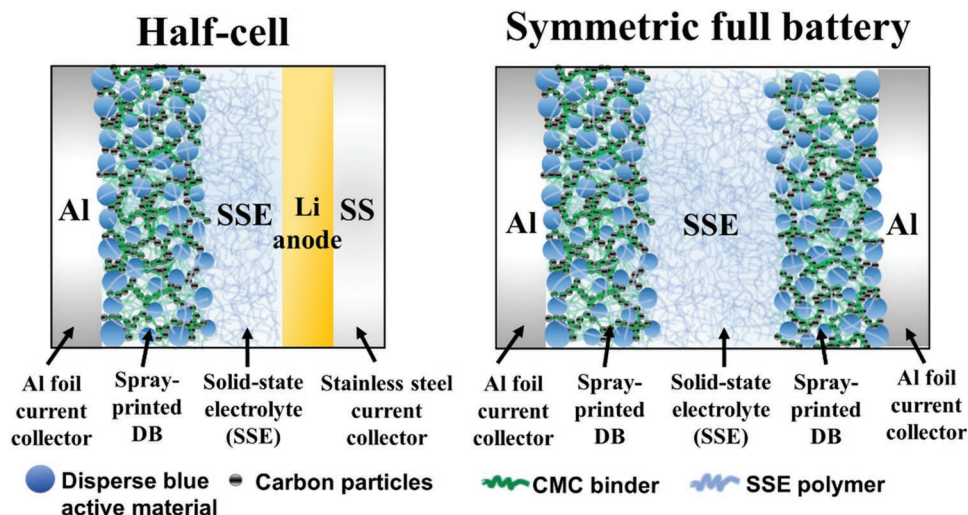


**Figure 1.** Schematic diagram of the half- and full-cell (symmetric) configurations of spray-printed disperse blue 134 electrodes with porous honeycomb structures.

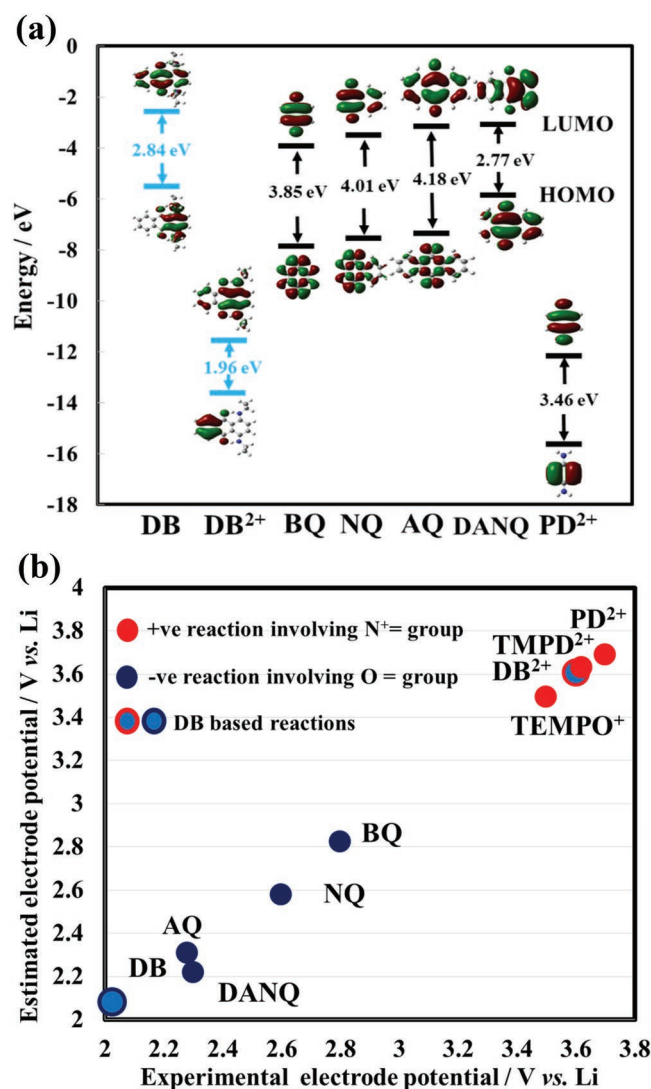
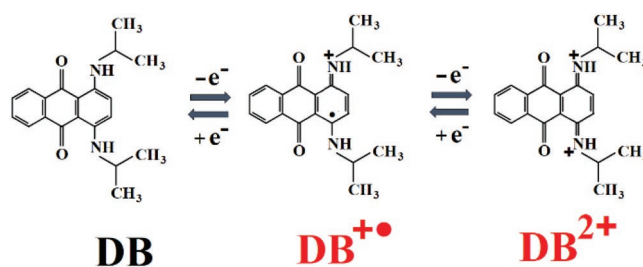


**Figure 2.** The molecular orbital energy levels of the disperse blue organic dye and other similar organic molecules obtained by DFT calculations: a) HOMO (or SOMO) and LUMO energy levels; and b) experimental electrode potentials versus calculated electrode potentials of organic molecules based on the method of Namazian et al.<sup>[25]</sup> where reduction is occurring on either the O= or N<sup>+</sup>= groups. Potentials of BQ and PD<sup>2+</sup> were calculated from Gibbs free energy (Supporting Information) and used as reference molecules for the reactions involving O= and N<sup>+</sup>= groups, respectively.

were first optimized and then used for calculating the highest occupied molecular orbitals (HOMO) (or singly occupied molecular orbital (SOMO) as half-filled HOMO) and the lowest unoccupied molecular orbitals (LUMO) in vacuum. In general, the overpotential required for the oxidation and reduction processes are related to the energy difference of the HOMO (or SOMO, of the reduced molecule) and the LUMO (of the oxidized molecule) from the relevant Fermi level.<sup>[23]</sup>

The calculated molecular orbital energies of the HOMO (or SOMO) and LUMO band of the various molecules considered in the oxidized (or neutral) states are summarized in Figure 2a. Calculated energies were similar to those previously reported



**Scheme 1.** Formations of radical cation and divalent cation through the oxidation of "disperse blue 134" (DB).

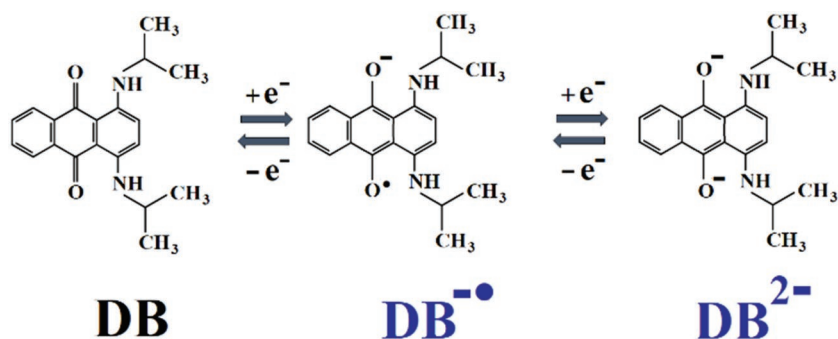
for benzoquinone (BQ), naphthoquinone (NQ), diamino-naphthoquinone (DANQ), and anthraquinone (AQ),<sup>[24]</sup> supporting the validity of the calculation approach. A relatively small HOMO–LUMO gap implies a lower overpotential for charge/discharge. Molecules containing amine or amino groups, i.e., disperse blue 134 (DB) and DANQ, had narrower bandgaps (<3 eV) than the other quinone molecules (>3.4 eV) because the strong electron-donating amino groups of DB and DANQ reduced the HOMO energy, thus decreasing the HOMO–LUMO gap.<sup>[24b]</sup>

The oxidized form of disperse blue 134 (DB<sup>2+</sup>) has not been studied in detail and proceeds in two one-electron steps<sup>[8]</sup> to form the radical cation (DB<sup>•+</sup>) then divalent cation (DB<sup>2+</sup>) as shown in Scheme 1.

The detailed reaction mechanisms supporting this hypothesis is provided in the Supporting Information (Figure S1, Supporting Information) and is similar to those proposed for a disperse violet 1 molecule<sup>[26]</sup> and other phenylenediamine-based molecules.<sup>[6]</sup> The radical cation in the first step was termed anthrasemiquinone (A<sup>•+</sup>),<sup>[26a]</sup> which facilitated further oxidation to the 2+ oxidation state due to the presence of two amine groups. Unlike most anthraquinones, the N atoms in the side ring of DB play a crucial role in enabling the molecule to be positively charged, as seen in cathodes based on TEMPO, *p*-phenylenediamine (PD), tetramethyl-*p*-phenylenediamine (TMPD).<sup>[6]</sup> The oxidation configuration was evident in the calculated HOMO and LUMO contours shown in Figure S2 (Supporting Information) that indicated the favored oxidation and reduction sites. When DB is neutral, the HOMO was localized on the side ring containing amine groups, which gives a higher tendency for subsequent oxidation to take place in this region.

The eigenvalues for HOMO and LUMO energies have a linear correlation with electrode potential and can provide more accurate estimations of electrode potentials of quinone molecules compared to conventional approaches involving the change of the Gibbs free energy of reaction.<sup>[25]</sup> For reduction reactions, i.e.,  $Q + 2e^- \rightarrow Q^{2-}$ , and  $Q^{2+} + 2e^- \rightarrow Q$ , the calculated LUMO energy is plotted against the experimental electrode potential for reduction for DB and related molecules in Figure S3 (Supporting Information).<sup>[24]</sup> The LUMO energy varied linearly with the electrode potential. Reduction of the oxidized DB molecule ( $DB^{2+} + 2e^- \rightarrow DB$ ) occurred at similar electrode potentials (>3.5 V vs Li) to the  $TEMPO^+ + e^- \rightarrow TEMPO$  and  $PD^{2+} + 2e^- \rightarrow PD$  that similarly to DB also contained N atoms. Based on the methods of Namazian et al.,<sup>[25]</sup>





**Scheme 2.** Formation of a radical anion and then divalent anion through the reduction of the “disperse blue 134” (DB) molecule.

the estimated electrode potentials for these organic molecules are reasonably close to the experimental values with deviations of less than 90 mV as shown in Figure 2b.

The reduction of the DB molecule is shown schematically in **Scheme 2** with the detailed reaction mechanism given in the Supporting Information (Figure S4, Supporting Information). This reaction is the same as most quinone molecules studied for electrode applications.<sup>[2]</sup>

The calculated electrode potential of the DB molecule in Figure 2b was more negative than most quinone molecules,<sup>[2]</sup> taking account that most of them have been described for cathode applications rather than anode applications. Anthraquinone is more electronegative than benzoquinone and naphthoquinone counterparts. Incorporation of amino groups is known to shift the negative potential up to 200 mV more negative.<sup>[24b,27]</sup> The potential difference ( $\approx 1.6$  V) between the  $\text{DB}^{2-}/\text{DB}$  ( $\approx 3.6$  V vs Li) and  $\text{DB}/\text{DB}^{\bullet-}$  reactions ( $\approx 2.0$  V vs Li) is sufficiently large to suggest feasibility for a symmetric battery application where both anode and cathode comprise the same active material (DB).

The optimized structures were further investigated for the charge on each atom for the DB molecule in reduced ( $\text{DB}^{\bullet-}$ ), neutral (DB), and oxidized states ( $\text{DB}^{2+}$ ) as shown in **Figure 3**. On the basis of Mulliken population analysis,<sup>[28]</sup> red and green are used to represent excess negative and positive charges respectively. The summation of the charges corresponded to the overall molecular charge state, i.e., the molecular charge is more negative (or more positive) at its reduced (or oxidized) state compared with the neutral state. However, as shown in Figure 3a, at the reduced state ( $\text{DB}^{\bullet-}$ ), the side ring with no functional group had a greater proportion of positive charge than in the neutral state, while the two aromatic rings with carboxyl and amine functional groups had significantly more negative charge. When the molecule was oxidized to  $2+$ , the central ring became more negatively charged, while the positive charge of the two side rings increased. The highest positive charge density was adjacent to the N atom in the side ring.

Electrostatic potential (ESP) contour mapping was used to indicate the likely interactions of the DB molecule with ions in an electrolyte. Regions with a positive ESP (red) had a higher tendency for nucleophilic reactions while electrophilic reactions were more favorable in regions of more negative ESP (blue). When the molecule was reduced, the regions near the carboxyl groups in the central ring and side ring (without the amine

groups) had negative ESP and were likely regions for the uptake of  $\text{Li}^+$ . On the other hand, the oxidized molecule had positive ESP concentrated only in the aromatic rings containing O and N atoms and were likely sites for interacting with anions, particularly  $\text{TFSI}^-$  (Figure 3b). Thus, the reduced and oxidized forms of DB suggested a tendency to interact and neutralize two  $\text{Li}^+$  cations and  $\text{TFSI}^-$  anions, respectively, as the charges formed at the electrodes are compensated by electrolyte ions. The estimated geometries and the corresponding charge and ESP distributions of molecules after neutralization are shown in **Figure 4a**. The Cartesian

coordinates of these neutralized molecules are available in Tables S1 and S2 (Supporting Information).

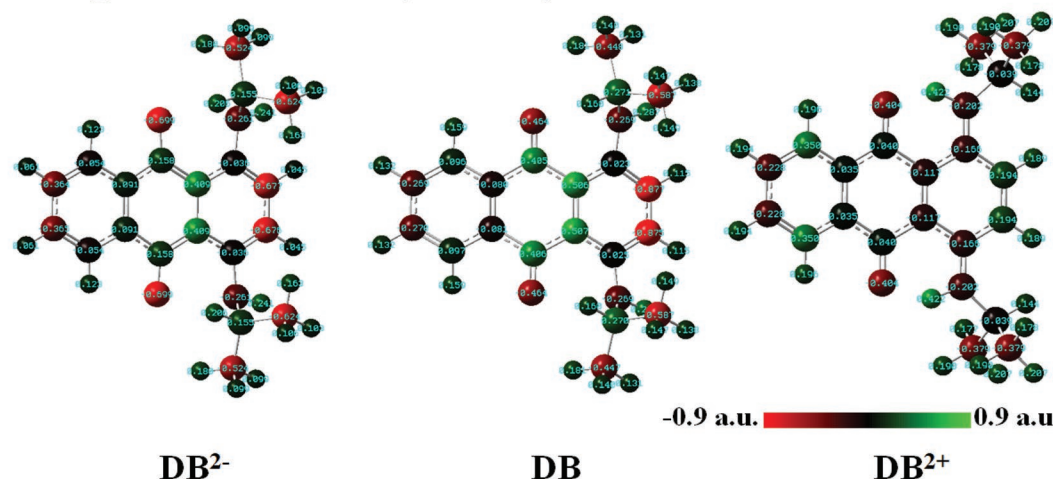
The oxidized DB molecule in the presence of LiTFSI salts was also characterized in deuterated acetone by  $^1\text{H}$  NMR spectroscopy as shown in Figure 4b. The  $^1\text{H}$  NMR spectrum was analyzed with the self-consistent field (SCF) gauge-including atomic orbital (GIAO) NMR chemical shielding method based on the estimated geometry of the neutralized DB molecule with two  $\text{TFSI}^-$  anions using DFT calculations. The signals at  $\delta$  7.22–7.49 were due to the aromatic protons, whereas the broad signal at  $\delta$  2.98 and multiplet at  $\delta$  3.96 corresponded to the protons of the amine groups and the isopropyl protons, respectively. The signals between  $\delta$  1 and 2 were related to a number of protons involved in methyl groups. Compared to the neutral DB, the chemical shift of the protons of the amine and methyl groups indicated reduced electron density in the hydrogen orbital. This suggested a more positive charge in those regions, which was broadly consistent with the insight provided by the DFT calculations. Furthermore, the formation of the N = group of the oxidized molecule was also identified by Fourier transform infrared (FT-IR) spectra at adsorption band of  $\approx 1690\text{ cm}^{-1}$ , and as shown in Figure S7 (Supporting Information).

## 2.2. Porous Organic Electrodes

Porous organic electrodes based on DB without any additional treatment or subsequent procedures were investigated. Consistent with previous work but for inorganic materials,<sup>[22b,29]</sup> the use of two miscible fugitive carriers (water:ethanol at 60:40 vol%) allowed honeycomb porous electrodes to be fabricated reproducibly over large areas, as shown in the scanning electron microscope (SEM) image at different magnifications in **Figure 5**. At higher magnifications ( $\times 2500$  magnification or higher, Figure S8, Supporting Information), the morphologies were still relevant to those obtained by slurry casting, suggesting similar material properties at micro scale. The evolution of electrode morphology at different fugitive water:ethanol ratios is shown in Figure S9 (Supporting Information), emphasizing the critically of the correct ratio to ensure spontaneous honeycomb formation that persisted even up to electrode thicknesses of  $\approx 35\text{ }\mu\text{m}$ .

The porous electrodes comprised the organic dyes, fine-scale carbon black particles, and binder (Figure S10, Supporting Information). The relatively high fraction of nanosized

## Charge distribution (atoms)



## Electrostatic potential distribution (surface)

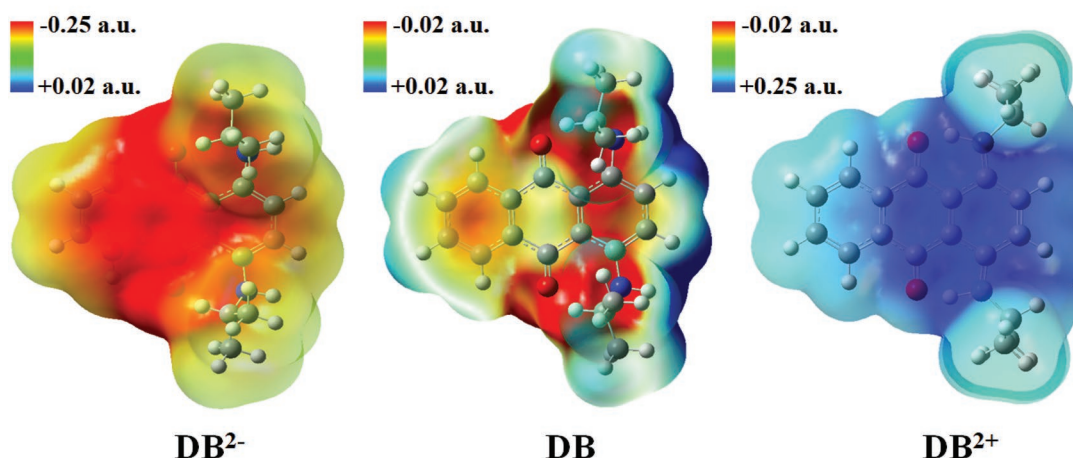


**Figure 3.** Mulliken charge and electrostatic potential distributions for the DB molecule in the reduced, neutral and oxidized forms obtained by DFT calculations. Enlarged graphs of Mulliken charge distribution of atoms are available in the Supporting Information (Figure S5, Supporting Information).

C additives (40 wt%), typical of organic-based electrodes, were generally well-dispersed and without obvious agglomeration. The CMC binder fraction (10 wt%) was also similar to those used in most quinone based organic cathodes.<sup>[2]</sup> In the presence of CMC, the dissolution rate of the electrode was 6 times less when immersed in excess amount of acetone solvents (Figure S11a, Supporting Information). However, as in most previous works, there was some residual dissolution of the DB observed in the first 60 h after which it tended to stabilize (Figure S11b, Supporting Information).

### 2.3. The Solid-State Electrolyte

Once the porous DB electrode was deposited, the SSE-based solution was immediately spray printed on top. Figure 6a shows

a SEM cross-sectional image of the resulting electrode with the SSE layer on the top and corresponding EDS maps for C, Al, S, F, and N. The electrode was  $\approx 30\ \mu\text{m}$  in thickness and both layers were relatively dense. The polymer based electrolyte was distinguished by the EDS by the S and F elements that originated only from the SSE. The SSE infiltrated into and through the porous electrode, down to the current collector.

The PIL-based SSE used here should not be confused with conventional gel polymers that contain a high liquid fraction ( $>70\ \text{wt}\%$ ) and typically suffer from progressive drying-out and a lack of stability.<sup>[18]</sup> The PIL-based SSE is also different from other IL-based gel polymers used for SSEs, usually known as “ionogels” that blend of ionic liquids with polar polymers such as PEO, PAN, PMA, PVDF-HFP, or by in situ polymerization of the ILs.<sup>[19b,30]</sup> The key distinction here is that the PIL-based SSE was entirely composed of organic molten salts, i.e., with TFSI<sup>-</sup>

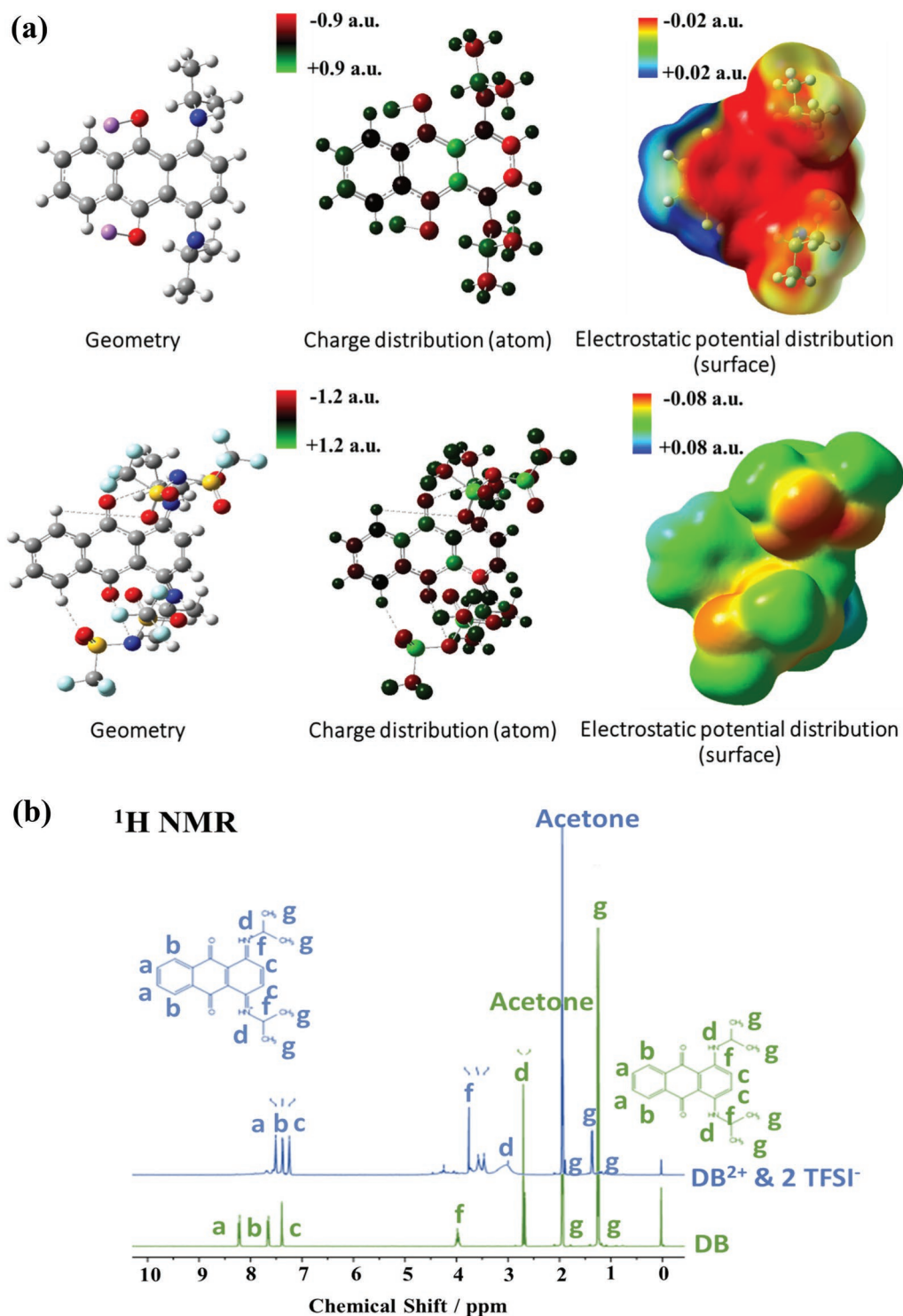


**Figure 4.** The interactions of the DB molecule with the electrolyte ions: a) Geometry, Mulliken charge distributions and electrostatic potential distributions of the neutralized DB molecule with  $\text{Li}^+$  cation and  $\text{TFSI}^-$  anions; b)  $^1\text{H}$  NMR spectra of the neutral DB and the oxidized DB dissolved in deuterated acetone with LiTFSI salt.

that provides electrostatic interaction to stabilize the IL within the polymer matrix. The stability of the PIL-based SSE was investigated by differential scanning calorimetry (DSC) (Figure S12, Supporting Information), as it was heated from  $-100$  to  $+100$  °C.

The trace for the PIL-based SSE and the PIL were closely similar and the PIL did not show a sharp endothermic (melting) peak of the IL at  $\approx -18$  °C, suggesting no phase separation and consistent with previous observations.<sup>[31]</sup> Therefore, compared



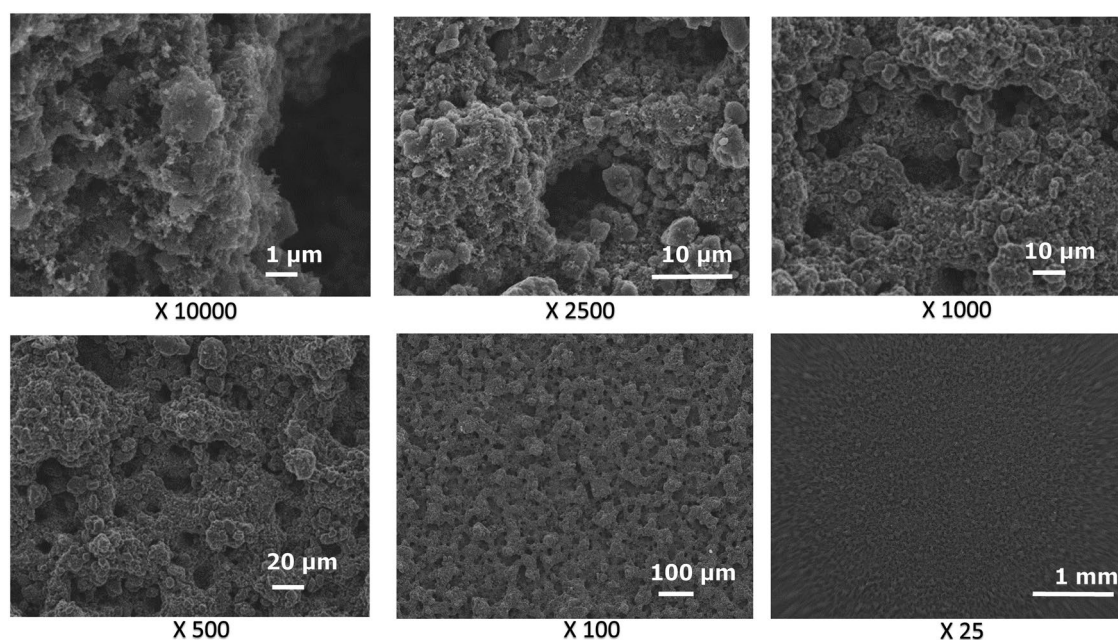


**Figure 5.** SEM micrographs of the DB-based spray printed electrodes with a honeycomb pore morphology.

with most conventional gel electrolytes, the high and stable miscibility with no phase separation suggested the PIL was particularly suitable for spray printing, where temperatures of 60 °C were required during drying.

For solid-state battery applications, the SSE should be electrochemically stable for both anode and cathode materials, typically from 0 to 4 V versus Li. The PIL-based SSE electrochemical stability was investigated by linear sweep voltammetry from open-circuit potential ( $\approx 2.7$  V vs Li) toward more negative or positive electrode potentials where any relative increase in current density might correspond to decomposition of the SSE. The inset of Figure 6b shows a plot of current density versus Li potential from  $-0.25$  to 7 V, indicating good electrochemical stability up to 5.5 V versus Li, with current densities of less than  $0.5 \text{ mA cm}^{-2}$  and in good agreement with similar electrolyte compositions.<sup>[19a]</sup> Similar pyrrolidinium-based ILs to those studied here tend to have higher electrochemical stability than their imidazolium counterparts (usually less than 5 V vs Li<sup>[32]</sup>).

The as-spray printed PIL-based SSE ionic conductivity was evaluated as a function of temperature as shown in Figure 6b. The ionic conductivity at  $20 \pm 1$  °C was  $2.1 \times 10^{-4} \text{ S cm}^{-1}$  that increased to  $\approx 10^{-2} \text{ S cm}^{-1}$  at temperatures higher than 70 °C, and was thus comparable or slightly higher than previously obtained for similar PILs and ILs.<sup>[19a,33]</sup>

Since ILs have a relative high viscosity (i.e.,  $>10$  cP), their ionic conductivities are often an order of magnitude lower than those of conventional carbonate-based electrolytes ( $>10^{-2} \text{ S cm}^{-1}$ ). However, as summarized in a recent review article,<sup>[19b]</sup> the ionic conductivities of most IL based ternary (or gel) electrolytes are rarely higher than  $\times 10^{-4} \text{ S cm}^{-1}$  at 20 °C. Overall, taking account of both safety, volatility, phase separation, and ionic conductivity aspects, the PIL-based SSE had an attractive balance of properties.

## 2.4. Electrode Reactions with the SSE

To evaluate the possibility for the DB electrode plus PIL SSE system to be used for a symmetric all-organic battery, the electrode potential was swept over a wide potential range ( $+1.3$  to  $+4.3$  V vs Li) that spanned both the negative and positive electrode reactions suggested by previous work and the DFT calculations. The starting electrode condition was in the as-spray neutral state with an open circuit potential of 2.7–2.8 V versus Li. The individual voltammograms for both negative and positive electrode reactions were obtained by sweeping at  $0.5 \text{ mV s}^{-1}$  from this potential toward more negative ( $+1.3$  V vs Li) or more positive ( $+4.3$  V vs Li) potentials, respectively.

As shown in Figure 7a, the DB-based electrode exhibited multielectron transfers as characterized by a number of distinct peaks in the voltammogram(s). Each pair of cathodic and anodic peaks represented a quasi-reversible reaction with at least one electron-transfer(s). There were two pairs of peaks at  $\approx +3.35$  and  $\approx +3.85$  V versus Li in the more positive potential region ( $+2.7$  to  $+4.3$  V vs Li). Since these potentials were more positive than the initial open-circuit potential value ( $\approx +2.7$  V vs Li), DB was oxidized in two one-electron steps to form radical cations (DB<sup>•+</sup>) and divalent cations (DB<sup>2+</sup>), consistent with structures described early for the HOMO state (Figure S2, Supporting Information) and shown in Scheme 1.

For this positive electrode reaction, the voltammetric behavior was in good agreement with previous works using the same or similar diaminoanthraquinone dye molecules.<sup>[8,26a]</sup> DB oxidation alone was also investigated at scan rates between 0.3 and  $1.3 \text{ mV s}^{-1}$  as shown in Figure 7b. As expected, the peak separation and current intensity increased at faster scan rates. The anodic peak current gave a good best-linear fit to the square root of the scan rate (Figure S13, Supporting Information) that

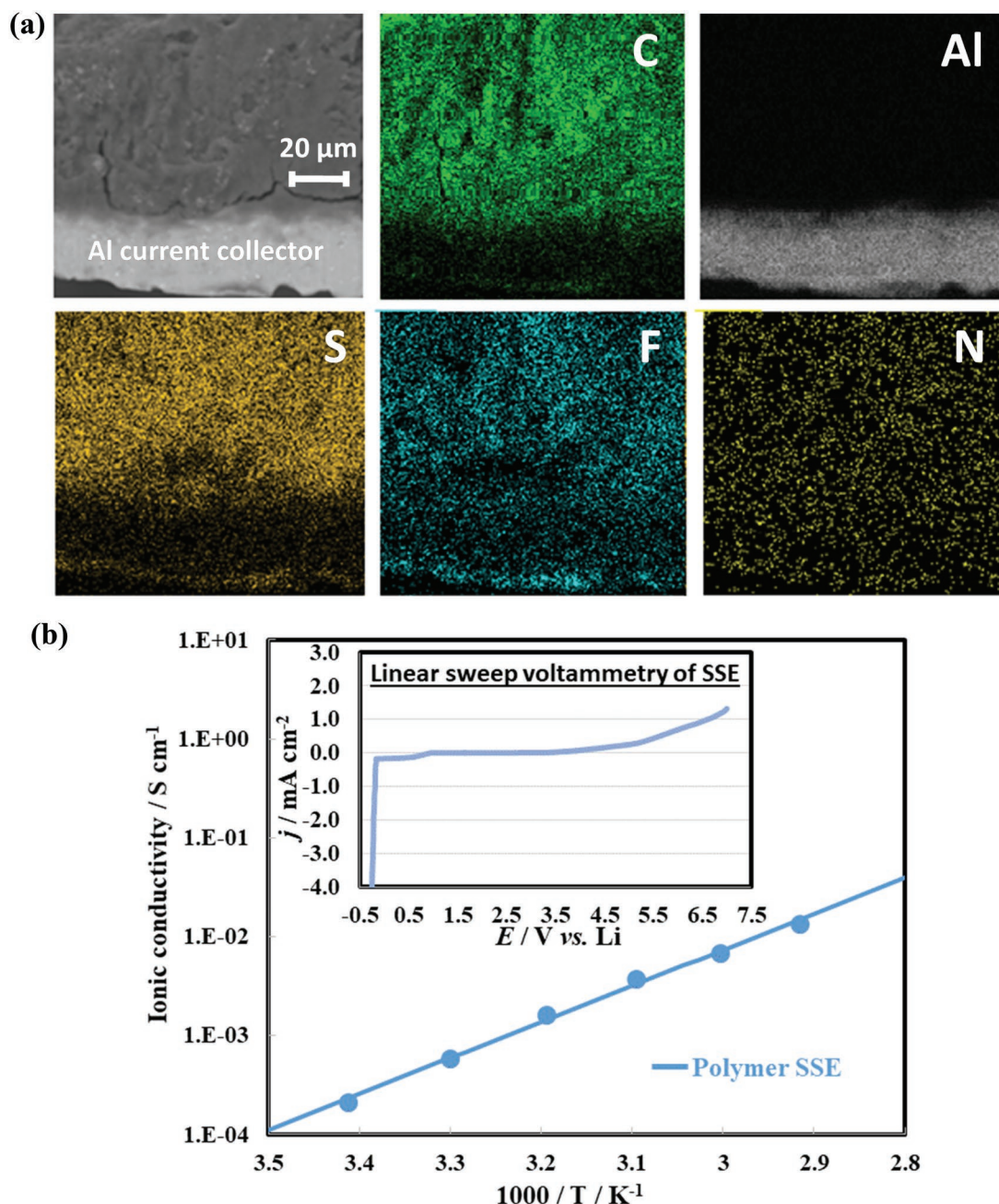


**Figure 6.** a) SEM cross-sectional micrographs and associated EDS elemental maps of a spray printed DB-based porous electrode infiltrated with a PIL based solid-state electrolytes; b) ionic conductivity and electrochemical stability of the PIL SSE at temperatures between 20 and 70 °C (inset: linear sweep voltammogram obtained at 1 mV s<sup>-1</sup> and 22 °C). Ionic conductivity measurements were by EIS using a stainless steel/SSE/stainless steel coin cell arrangement, while linear sweep voltammetry was conducted using a stainless steel/SSE/Li coin cell.

suggested that the anodic reaction was controlled by the diffusion of the TFSI<sup>-</sup> anions.<sup>[34]</sup>

In the negative sweep region, the DB electrode was reduced in two one-electron steps as indicated by two pairs of cathodic and anodic peaks (Figure 7a). In the less positive potential region (+1.3 to +2.7 V vs Li), the two anodic peaks were somewhat indistinct and overlapping. However, this reduction reaction is well-documented and widely used in most quinone-based batteries.<sup>[2]</sup> With reference to a similar voltammogram but for DB

dissolved in the IL (i.e., not the polymerized version used here) and conventional propylene carbonate electrolytes used in Li-ion batteries, Figure S14 (Supporting Information) shows two pairs of peaks for radical anion (DB<sup>•-</sup>) and divalent anions (DB<sup>2-</sup>) identified at ≈1.8 and ≈2.25 V versus Li, respectively. These potentials were again comparable with those of typical anthraquinones.<sup>[1,2]</sup> For this two electron-transfer reduction, one pair of overlapping cathodic and anodic peaks were also observed in previous work using both anthraquinone and a SSE.<sup>[35]</sup>



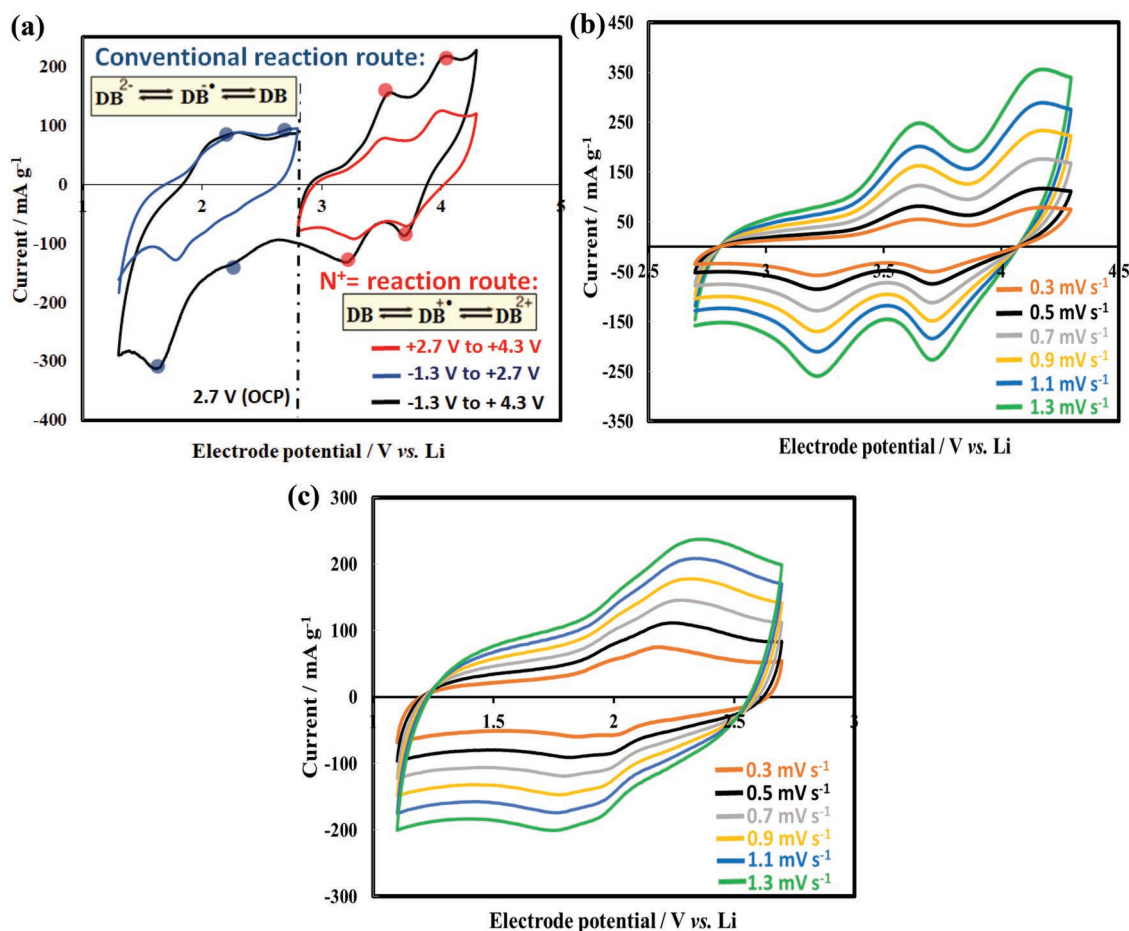


**Figure 7.** Cyclic voltammograms of the DB porous electrodes (half-cells) with PIL-based SSE. a) Three sets of potential ranges covering the negative and positive electrode reactions at a sweep rate of  $0.5 \text{ mV s}^{-1}$ ; effect of the sweep rate on b) the positive electrode reaction (2.7–4.3 V vs Li); and c) the negative electrode reaction (1.3–2.7 V vs Li).

The reduction of the DB electrode was investigated at different scan rates as shown in Figure 7c, and reactions again determined to be diffusion controlled. Compared with the oxidation process, the peak current of the reduction reaction was lower, which may be due to the lower concentration of cations ( $\text{Li}^+$ ) than anions ( $\text{TFSI}^-$ ) in the PIL-based SSE. The migration of mobile ions and charge neutralization are generally considered as a problematic, limiting factor for all-organic batteries.<sup>[28]</sup> Taking account of the salt concentrations in the SSE, the diffusion coefficient of  $\text{TFSI}^-$  was estimated to be  $\approx 1.1 \times 10^{-11} \text{ cm}^2 \text{ s}^{-1}$  by averaging the two anodic peaks through the oxidation route (assuming  $3.6 \text{ M TFSI}^-$  and one electron-transfer per peak). The diffusion coefficient of  $\text{Li}^+$  was estimated as  $\approx 1.2 \times 10^{-11} \text{ cm}^2 \text{ s}^{-1}$  based on the overlapping peak in the reduction process (assuming  $0.7 \text{ M Li}^+$  and two electron-transfers per peak) but with less molecular weight. The diffusion coefficients of these radical reactions are relatively fast compared with ion (de)intercalation reactions.<sup>[2]</sup>

## 2.5. Half-Cell Charge-Discharge Cycling

In the neutral, discharged state with an open-circuit potential of  $\approx 2.7$ – $2.8 \text{ V}$  versus Li electrodes were charge-discharge cycled

in a half-cell configuration using the same potential ranges as in the voltammetric study. **Figure 8** shows the positive and negative half-cell cycling performance at C-rates ranging from 0.2 to 5 C. By assuming two electron-transfers and a molecular weight of  $322.4 \text{ g mol}^{-1}$ , the theoretical capacity was estimated as  $166 \text{ mA h g}^{-1}$ .

Both half-cells were initially charge-discharge cycled at 0.5 C for 50 cycles, followed by cycling at different C-rates (each C-rate for 20 cycles) for another 100 cycles. The charge and discharge capacities decreased rapidly in the early cycles and tended toward stability after 40 to 50 cycles. The rapid decrease in capacity was due to the dissolution of disperse blue dye into the solid-state electrolyte,<sup>[2]</sup> especially in the first 60 h (Figure S11b, Supporting Information). However, both discharge capacity and dissolution of organic dye tended to stabilize after time. This shows that the capacity fading was associated with the dissolutions of the organic dye.

For both negative and positive electrode reactions, the capacity in the first cycles was  $110$  to  $120 \text{ mA h g}^{-1}$  (Figure S15, Supporting Information), which corresponded to an active material utilization of 66% to 72% and typical of quinone-based batteries but using conventional liquid electrolytes, suggesting effective infiltration of the SSE, and that effective

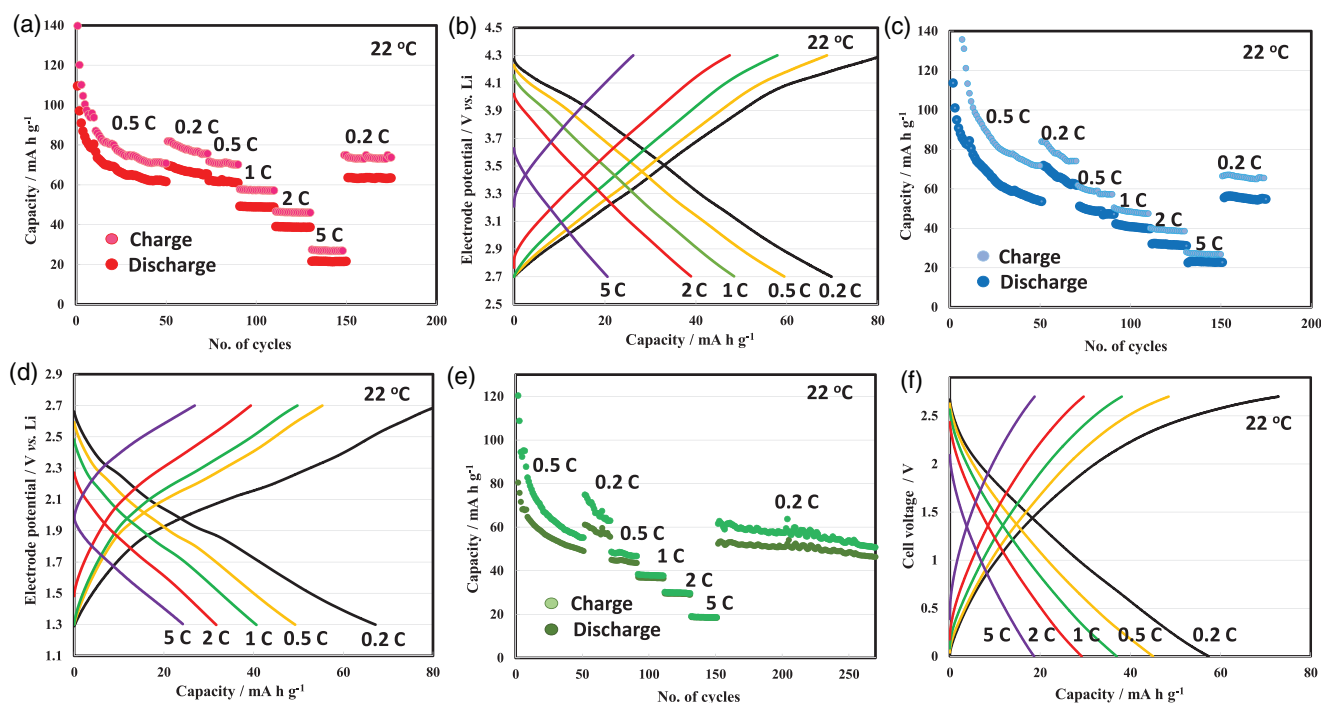


**Figure 8.** Half- and full-cell charge-discharge cycling performance of DB-based electrodes with a PIL-based SSE at C-rates 0.2, 0.5, 1, 2, and 5 C. Positive half-cell electrode reaction: a) charge-discharge capacities; b) electrode potential profile; Negative half-cell electrode reactions: c) charge-discharge capacities; d) electrode potential profile; Full-battery reaction: e) charge-discharge capacities; f) voltage profiles. Porous electrode thickness  $\approx 30 \mu\text{m}$ , operating at  $22^\circ\text{C}$ .

material/electrolyte interfacial contact was reasonably well sustained. Nonetheless, the capacity faded to 55 to  $60 \text{ mA h g}^{-1}$  (at 0.5 C) after 50 cycles. Similar capacity losses have also been reported for most unpolymersized quinone molecules.<sup>[2,7,35,36]</sup> For example, a 9,10-anthraquinone with a solid electrolyte (PEO with  $\text{Li}^+$  salts) lost nearly 30% capacity after 50 cycles at a lower rate of  $<0.1 \text{ C}$ .<sup>[35]</sup>

The charge-discharge profiles in Figure 8b,d show a potential plateau in the first few cycles (Figure S15, Supporting Information) that gradually became inclined profiles in following cycles. These plateaux are related to peaks in the cyclic voltammograms in Figure 7a. For the positive and negative half-cells, at 0.2 C (after more than 50 cycles), the average reduction potentials were  $\approx 3.45$  and  $\approx 1.85 \text{ V}$  versus Li respectively. For the same sets of cycles, the oxidation potentials were  $\approx 3.65$  and  $\approx 2.15 \text{ V}$  versus respectively. Both capacities and potentials decreased at higher C-rates but with coulombic efficiencies of more than 80% (Figure 8b and Figure S16, Supporting Information). The positive electrode reactions had a more stable performance in terms of capacity and overpotential, which was likely due to a higher fraction of TFSI<sup>-</sup> anion than  $\text{Li}^+$  cation in the SSE, as discussed earlier. This also suggested that the negative electrode reaction would likely be the limiting reaction in a full-cell configuration. The positive electrode potential due to  $\text{DB}^{2+}$  ( $\approx 3.5 \text{ V}$ ) was among the highest for quinones<sup>[2]</sup> (Figure S17, Supporting Information) and comparable with those of nitroxide radicals ( $<3.8 \text{ V vs Li}$ ) that are used in organic radical batteries.<sup>[37]</sup> On the other hand, the negative electrode reaction of  $\text{DB}^{2-}$  exhibited one of the lowest

electrode potentials ( $\approx 2.0 \text{ V}$ , Figure S17, Supporting Information) amongst the quinones.<sup>[2]</sup>

## 2.6. Full-Cell Charge-Discharge Cycling

A full symmetric cell configuration was assembled by pressing two spray printed DB-based porous electrodes with SSE coatings against one another. The initial open-circuit voltage was close to 0 V prior to any reaction process. On the basis of the half-cell electrode reactions, the full battery was charge-discharge cycled between 0 and 2.7 V. Figure 8 shows the resulting behavior in terms of capacities and voltage profiles at C-rates ranging from 0.2 to 5 C. Similar to the half-cell studies, the full battery was initially charge-discharge cycled at 0.5 C for 50 cycles, followed by cycling at different C-rates (each C-rate for 20 cycles) for another 100 cycles. After these 150 cycles, the battery was also further cycled for 120 more cycles at 0.2 C. The initial discharge capacity was  $\approx 80 \text{ mA h g}^{-1}$  at 0.5 C and decreased to  $\approx 50 \text{ mA h g}^{-1}$  after 50 cycles, lower than the equivalent half-cells. This was due to the narrower voltage window required for electrochemical stability than used in the half-cell studies. A benefit of the narrower voltage range was an improvement in the coulombic efficiency ( $>80\%$ ) and capacity retention ( $\approx 62\%$ ) over equivalent half-cell performance (Figure 8 and Figure S16, Supporting Information).

The porous electrodes in this work enabled large and effective material/electrolyte interfacial contact, but also promoted the dissolution rate of the organic dye materials, and resulted

in a more significant capacity fading and lower coulombic efficiencies than nonporous electrodes (Figure 8 and Figure S16, Supporting Information). However, both tended to stabilize with the dissolution of organic dye after certain period of time (i.e., after  $\approx 60$  h). The coulombic efficiency of a similar nonporous electrode was more than 90% with the solid-state electrolyte (Figure S18, Supporting Information), comparable with those obtained in prior works.<sup>[2]</sup> Despite the lower coulombic efficiencies, porous electrodes allowed more effective infiltration of the PIL-based SSE and delivered  $\approx 48\%$  more discharge capacity than their nonporous counterparts, for electrode thicknesses of up to 30  $\mu\text{m}$  (Figure S18, Supporting Information).

At 0.2 C and after 50 cycles, the average charge and discharge voltages were  $\approx 2.0$  and  $\approx 1.1$  V, respectively, and for different C-rates, the capacities were similar to the negative half-cell. Since there was no (de)intercalation involved in the battery reactions (Figure S19, Supporting Information), the battery could charge-discharge at up to 5 C, implying a comparatively low charge transfer resistance, i.e., good contact between the SSE and the DB, facilitated by the infiltrated porous electrode configuration.

Although essentially a proof-of-concept system for an all-organic solid-state symmetric cell, the preliminary performance was nonetheless comparable with many symmetric metal-based batteries using SSEs<sup>[14]</sup> such as Fe-doped  $\text{Li}_3\text{V}_2(\text{PO}_4)_3$  electrodes using a  $\text{Li}_{1.5}\text{Al}_{0.5}\text{Ge}_{1.5}(\text{PO}_4)_3$  SSE that provided  $78 \text{ mA h g}^{-1}$ ,<sup>[38]</sup> and most all-organic batteries based on liquid electrolytes that operated between 1 and 1.8 V and delivered 40–200  $\text{mA h g}^{-1}$ .<sup>[39]</sup> The performance was comparable to several recent lithium–organic batteries<sup>[18,40]</sup> and “metal-based” lithium-ion batteries using SSEs ( $<100 \text{ mA h g}^{-1}$  at room temperature),<sup>[41]</sup> as well as aqueous batteries ( $<80 \text{ mA h g}^{-1}$  at room temperature) based on Prussian Blue analogue electrodes.<sup>[42]</sup>

The symmetric solid-state organic battery did not involve Li deposition or use of flammable electrolytes, and fabrication was a rapid single-step procedure. It is also worth noting the DB textile dye molecule (disperse blue 134) is considered a relatively safe material, which is neither toxic, corrosive, flammable nor hazardous to humans or the environment, which may be attractive for grid-scale and electric vehicle applications, considering its suitability for mass production, effective recycling, and high intrinsic safety.

### 3. Conclusions

A symmetric all-organic solid-state battery cell based on a commercial dye molecule and a polymer ionic liquid based electrolyte with high stability has been proposed. The battery was prepared by using a scalable spray-printing technique,<sup>[43]</sup> in which a porous organic electrode was deposited as the first layer, and a nonflammable PIL-based SSE was subsequently spray-printed. This proof-of-concept system was evaluated through half- and full-cell charge-discharge cycling.

Using DFT-based calculations, the active dye molecule that comprised an amine group in the side ring and a carboxyl group in the central ring was shown to be capable of forming

cations and anions. The formation of these cations and anions supported the idea in principle that the same molecule could be used in both negative and positive electrode reactions, exhibiting two-electron transfers with quasi-reversibility and a low HOMO–LUMO bandgap of  $<3$  eV. DFT calculations and charge-discharge experiments revealed potentials for the negative and positive electrode reactions of  $\approx 2.0$  and  $\approx 3.5$  V versus Li, respectively, which were among the lowest and highest reported for quinone molecules.

The resulting full-battery was charge-discharge cycled at different C-rates (0.2 to 5 C) for 250 cycles. The discharge cell voltages were more than 1 V regardless of C-rate. However, the discharge capacity faded from  $\approx 80 \text{ mA h g}^{-1}$  (first cycle) to  $\approx 50 \text{ mA h g}^{-1}$  at 0.5 C after 50 cycles. Additional approaches, i.e., polymerization, are therefore necessary to address the capacity fading by reducing the dissolution rate of the active molecule.

### Supporting Information

Supporting Information is available from the Wiley Online Library or from the author.

### Acknowledgements

The authors would like to thank the UK Engineering and Physical Sciences Research Council (“Enabling next generation lithium batteries” EP/M009521/1), CONACYT-SENER Sustentabilidad Energetica, and the Royal Society for their financial support. The color scheme in Figure 8e was changed on October 17, 2019.

### Conflict of Interest

The authors declare no conflict of interest.

### Keywords

organic batteries, porous electrodes, solid-state batteries, spray-printing, symmetric electrodes

Received: April 30, 2019

Revised: June 6, 2019

Published online: September 8, 2019

- [1] A. Mauger, M. Armand, C. M. Julien, K. Zaghib, *J. Power Sources* **2017**, 353, 333.
- [2] a) Y. Wu, R. Zeng, J. Nan, D. Shu, Y. Qiu, S.-L. Chou, *Adv. Energy Mater.* **2017**, 7, 1700278; b) B. Hupler, A. Wild, U. S. Schubert, *Adv. Energy Mater.* **2015**, 5, 1402034.
- [3] a) A. Vizintin, J. Bitenc, A. K. Lautar, K. Pirnat, J. Grdadolnik, J. Stare, A. Randon-Vitanova, R. Dominko, *Nat. Commun.* **2018**, 9, 661; b) R. Emanuelsson, M. Sterby, M. Strømme, M. Sjödin, *J. Am. Chem. Soc.* **2017**, 139, 4828.
- [4] B. Lee, Y. Ko, G. Kwon, S. Lee, K. Ku, J. Kim, K. Kang, *Joule* **2018**, 2, 61.
- [5] a) J. Huang, B. Pan, W. Duan, X. Wei, R. S. Assary, L. Su, F. R. Brushett, L. Cheng, C. Liao, M. S. Ferrandon, W. Wang, Z. Zhang, A. K. Burrell, L. A. Curtiss, I. A. Shkrob, J. S. Moore,



- L. Zhang, *Sci. Rep.* **2016**, 6, 32102; b) H. Nishide, S. Iwasa, Y.-J. Pu, T. Suga, K. Nakahara, M. Satoh, *Electrochim. Acta* **2004**, 50, 827.
- [6] a) E. Deunf, P. Moreau, E. Quarez, D. Guyomard, F. Dolhem, P. Poizot, *J. Mater. Chem. A* **2016**, 4, 6131; b) E. Deunf, F. Dolhem, D. Guyomard, J. Simonet, P. Poizot, *Electrochim. Acta* **2018**, 262, 276.
- [7] a) V. Vatanen, J. M. Eloranta, M. Vuolle, *J. Chem. Soc. Perkin Trans. 2* **1998**, 2, 2483; b) K. Piech, T. Bally, T. Ichino, J. Stanton, *Phys. Chem. Chem. Phys.* **2014**, 16, 2011.
- [8] R. A. Potash, J. R. McKone, S. Conte, H. D. Abruña, *J. Electrochem. Soc.* **2016**, 163, A338.
- [9] J. Barker, R. K. B. Gover, P. Burns, A. Bryan, *Electrochem. Solid-State Lett.* **2005**, 8, A285.
- [10] J. C. Burns, L. J. Krause, D. B. Le, L. D. Jensen, A. J. Smith, D. J. Xiong, J. R. Dahn, *J. Electrochem. Soc.* **2011**, 158, A1417.
- [11] a) W. Wang, L. J. Wang, Z. Q. Zhu, Z. Hu, Q. Zhao, J. Chen, *Angew. Chem., Int. Ed.* **2014**, 53, 5892; b) S. Wang, L. Wang, K. Zhang, Z. Zhu, Z. Tao, J. Chen, *Nano Lett.* **2013**, 13, 4404.
- [12] L. M. Zhu, A. W. Lei, Y. L. Cao, X. P. Ai, H. X. Yang, *Chem. Commun.* **2013**, 49, 567.
- [13] X. Chi, Y. Liang, F. Hao, Y. Zhang, J. Whiteley, H. Dong, P. Hu, S. Lee, Y. Yao, *Angew. Chem., Int. Ed.* **2018**, 57, 2630.
- [14] L. Zhang, S. X. Dou, H. K. Liu, Y. Huang, X. Hu, *Adv. Sci.* **2016**, 3, 1600115.
- [15] J. N. Chakraborty, *Fundamentals and Practices in Colouration of Textiles*, 2nd ed., Woodhead Publishing, India **2014**, pp. 209–219.
- [16] a) P. Leung, A. A. Shah, L. Sanz, C. Flox, J. R. Morante, Q. Xu, M. R. Mohamed, C. Ponce de Leon, F. C. Walsh, *J. Power Sources* **2017**, 360, 243; b) P. Leung, D. Aili, Q. Xu, A. Rodchanarowan, A. A. Shah, *Sustainable Energy & Fuels* **2018**, 2, 2252.
- [17] a) Y. Hanyu, Y. Ganbe, I. Honma, *J. Power Sources* **2013**, 221, 186; b) Y. Hanyu, I. Honma, *Sci. Rep.* **2012**, 2, 453.
- [18] S. Liang, W. Yan, X. Wu, Y. Zhang, Y. Zhu, H. Wang, Y. Wu, *Solid State Ionics* **2018**, 318, 2.
- [19] a) A.-L. Pont, R. Marcilla, I. De Meatza, H. Grande, D. Mecerreyes, *J. Power Sources* **2009**, 188, 558; b) I. Osada, H. de Vries, B. Scrosati, S. Passerini, *Angew. Chem., Int. Ed.* **2016**, 55, 500.
- [20] a) J. Zheng, A. He, J. Li, J. Xu, C. C. Han, *Polymer* **2006**, 47, 7095; b) Y. Wu, R. L. Clark, *J. Colloid Interface Sci.* **2007**, 310, 529; c) G. R. Guillen, Y. Pan, M. Li, E. M. V. Hoek, *Ind. Eng. Chem. Res.* **2011**, 50, 3798; d) V.-T. Bui, V.-D. Dao, H.-S. Choi, *Polymer* **2016**, 101, 184.
- [21] Y. S. Zhu, S. Y. Xiao, M. X. Li, Z. Chang, F. X. Wang, J. Gao, Y. P. Wu, *J. Power Sources* **2015**, 288, 368.
- [22] a) C. Huang, P. S. Grant, *J. Mater. Chem. A* **2018**, 6, 14689; b) S. H. Lee, A. Mahadevegowda, C. Huang, J. D. Evans, P. S. Grant, *J. Mater. Chem. A* **2018**, 6, 13133.
- [23] R. Jamies, R. Cervantes-Alcala, W. Garcia-Garcia, M. Miranda-Hernandez, *Electrochim. Acta* **2018**, 284, 108.
- [24] a) Y. Ding, Y. Li, G. Yu, *Chem* **2016**, 1, 790; b) J. Lee, H. Kim, M. J. Park, *Chem. Mater.* **2016**, 28, 2408.
- [25] a) M. Namazian, H. A. Almodarresieh, M. R. Noorbala, H. R. Zare, *Chem. Phys. Lett.* **2004**, 396, 424; b) M. Namazian, *J. Mol. Struct.: THEOCHEM* **2003**, 664–665, 273.
- [26] a) V. Vatanen, J. A. Pedersen, *J. Chem. Soc. Perkin Trans. 2* **1996**, 2, 2207; b) V. Vatanen, J. M. Eloranta, M. Vuille, *Magn. Reson. Chem.* **1999**, 37, 774.
- [27] K. C. Kim, T. Liu, S. W. Lee, S. S. Jang, *J. Am. Chem. Soc.* **2016**, 138, 2374.
- [28] T. B. Woldeamanuale, *J. Phys. Chem. Biophys.* **2016**, 6, 100226.
- [29] a) S. H. Lee, K. Li, C. Huang, J. D. Evans, P. S. Grant, *ACS Appl. Mater. Interfaces* **2019**, 11, 603; b) S. H. Lee, C. Huang, C. Johnston, P. S. Grant, *Electrochim. Acta* **2018**, 292, 546.
- [30] Q. Zhao, W. Huang, Z. Luo, L. Liu, Y. Lu, Y. Li, L. Li, J. Hu, H. Ma, J. Chen, *Sci. Adv.* **2018**, 4, eaao1761.
- [31] a) C. Stolze, T. Janoschka, S. Flauder, F. A. Muller, M. D. Hager, U. S. Schubert, *ACS Appl. Mater. Interfaces* **2016**, 8, 23614; b) A. Ahmad, Q. Wang, S. Melhi, L. Mao, M. Zhang, B.-H. Han, K. Lu, Z. Wei, *Electrochim. Acta* **2017**, 255, 145.
- [32] W. A. Henderson, S. Passerini, *Chem. Mater.* **2004**, 16, 2881.
- [33] G. B. Appetecchi, G.-T. Kim, M. Montanino, M. Carewska, R. Marcilla, D. Mecerreyes, I. De Meatza, *J. Power Sources* **2010**, 195, 3668.
- [34] S. Muench, A. Wild, C. Friebe, B. Haupler, T. Janoschka, U. S. Schubert, *Chem. Rev.* **2016**, 116, 9438.
- [35] W. Li, L. Chen, Y. Sun, C. Wang, Y. Wang, Y. Xia, *Solid State Ionics* **2017**, 300, 114.
- [36] a) A. Lordache, V. Maurel, J.-M. Mouesca, J. Pecaut, L. Dubois, T. Gutel, *J. Power Sources* **2014**, 267, 553; b) L. Zhao, W.-K. Wang, A.-B. Wang, Z.-B. Yu, S. Chen, Y.-S. Yang, *J. Electrochem. Soc.* **2011**, 9, A991; c) Z. Song, Y. Qian, M. L. Gordin, D. Tang, T. Xu, M. Otani, H. Zhan, H. Zhou, D. Wang, *Angew. Chem., Int. Ed.* **2015**, 54, 13947.
- [37] T. Janoschka, M. D. Hager, U. S. Schubert, *Adv. Mater.* **2012**, 24, 6397.
- [38] Y. Kee, N. Dimov, E. Kobayashi, A. Kitajou, S. Okada, *Solid State Ionics* **2015**, 272, 138.
- [39] P. Poizot, F. Dolhem, J. Gaubicher, *Curr. Opin. Electrochem.* **2018**, 9, 70.
- [40] W. Wei, L. Li, L. Zhang, J. Hong, G. He, *Electrochem. Commun.* **2018**, 90, 21.
- [41] L. He, C. Chen, M. Kotobuki, F. Zheng, H. Zhou, L. Lu, *J. Mater. Chem. A* **2019**, 7, 9748.
- [42] a) R. A. Huggins, *J. Electrochem. Soc.* **2017**, 164, A5031; b) M. Pasta, C. D. Wessells, R. A. Huggins, Y. Cui, *Nat. Commun.* **2012**, 3, 1149.
- [43] a) C. Huang, P. S. Grant, *Sci. Rep.* **2013**, 3, 2393; b) C. Huang, N. Grobert, A. A. R. Watt, C. Johnston, A. Crossley, N. P. Young, P. S. Grant, *Carbon* **2013**, 61, 525.